Optica

Sub-cycle valleytronics: control of valley polarization using few-cycle linearly polarized pulses

Álvaro Jiménez-Galán,[1,*] Rui E. F. Silva,[2] Olga Smirnova,[1,3] and Misha Ivanov[1,4,5]

[1]*Max Born Institute, Max Born Strasse 2A, 12489 Berlin, Germany*
[2]*Dpto. Física Teórica de la Materia Condensada, Universidad Autónoma de Madrid, Madrid, Spain*
[3]*Technische Universität Berlin, Berlin, Germany*
[4]*Department of Physics, Humboldt University, Berlin, Germany*
[5]*Blackett Laboratory, Imperial College London, London, UK*
Corresponding author: jimenez@mbi-berlin.de

So far, it has been assumed that selective excitation of a desired valley in the Brillouin zone of a hexagonal two-dimensional material has to rely on using circularly polarized fields. We theoretically demonstrate a way to control the valley excitation in hexagonal 2D materials on a few-femtosecond timescale using a few-cycle, linearly polarized pulse with controlled carrier–envelope phase. The valley polarization is mapped onto the strength of the perpendicular harmonic signal of a weak, linearly polarized pulse, which allows to read this information all-optically without destroying the valley state and without relying on the Berry curvature, making our approach potentially applicable to inversion-symmetric materials. We show applicability of this method to hexagonal boron nitride and MoS$_2$.

Generation of few-cycle laser pulses with controlled electric field oscillations under the envelope, i.e., controlled carrier–envelope phase (CEP), catalyzed the development of attosecond physics and technology, providing tools to control electron dynamics on a sub-laser-cycle timescale [1,2]. Attosecond technology has now started to develop its potential in condensed matter, in particular via high harmonic generation (HHG) [3–8], including 2D materials [9–11]. The practical possibility of shaping individual oscillations of an optical laser pulse marks first steps towards lightwave electronics—the sub-cycle monitoring and steering of electronic dynamics in solids [12–14], which holds the potential to increase the speed of information processing from the current gigahertz to the petahertz rate (petahertz lightwave electronics.)

Almost simultaneously with the advent of CEP-controlled few-cycle pulses, the isolation of a single layer of graphene signaled a breakthrough in modern material science and condensed matter physics [15]. The fascinating electronic properties of graphene, with carriers following the massless Dirac equation at the two points of the Brillouin zone **K** and **K'**, led to a plethora of new physical phenomena such as the anomalous integer quantum

Hall effect and topological superconductivity [16]. Similar exotic properties were found also in graphene's insulating counterpart, i.e., hexagonal boron nitride (hBN) and in other 2D materials such as transition metal dichalcogenides (TMDs). One of the most promising aspects of these insulating 2D materials is their ability to support an extra electronic degree of freedom, i.e., the valley pseudospin, which labels the energy-degenerate extrema of the bands and can serve as an additional information carrier for information processing [17–19].

In hexagonal monolayers with broken inversion symmetry, the minimum band gap is located at the **K** and **K'** Dirac points [Fig. 1(a)], which form energy-degenerate valleys in the landscape of the valence and conduction bands [17]. For a model with one valence and one conduction band, the Bloch electrons carry equal but opposite orbital magnetic moment $m(\mathbf{k})$ in the neighborhood of the two valleys: $m(\mathbf{k}) = \frac{e}{2\hbar}\Omega(\mathbf{k})\varepsilon_g(\mathbf{k})$ [17]. Here, $\varepsilon_g(\mathbf{k}) = \varepsilon_c(\mathbf{k}) - \varepsilon_v(\mathbf{k})$ is the difference in energy dispersions between the two bands, and $\Omega(\mathbf{k})$ is the Berry curvature, which is normal to the monolayer and opposite in both valleys [Fig. 1(b)]. This leads to valley selection rules: right-circularly polarized photons couple to **K**, while left-circularly polarized photons couple to **K'** [17]. Hence, optical excitation with band-gap-resonant circular drivers generates a valley asymmetry and opens a way to use the valley pseudospin—the core idea of valleytronics. Helicity-induced valley initialization has been established with resonant circularly polarized drivers [20] and with single-cycle circular drivers [21]. Ultrafast coherent control of valley selection, i.e., switching between inducing excitation at **K** and at **K'** on timescales shorter than valley depolarization, is a major challenge, recently addressed using resonant, circular pump fields phase-locked to strong terahertz fields [22] and tailored pulses [23]. The wide variety of materials that can be used and combined for valleytronics demands non-material-specific methods for ultrafast valley switching, along with the development of optical measurement schemes of the valley polarization [18,19].

The valley selection rules suggest that linearly polarized light couples equally to both valleys, and it is widely accepted that valley polarization with linearly polarized fields is not possible
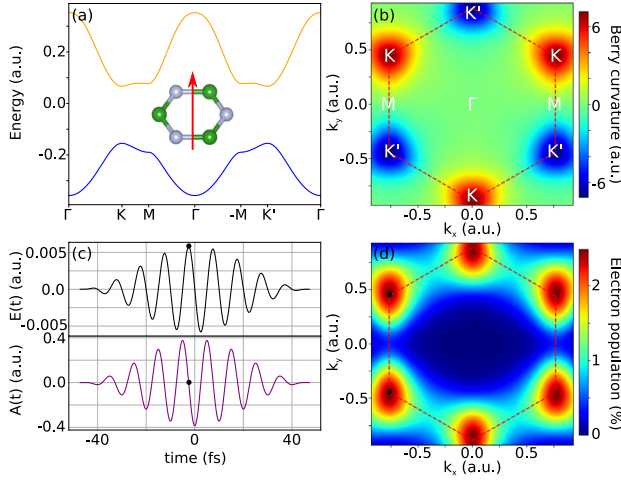
Fig. 1. (a) Energy and (b) Berry curvature of the first conduction band in hBN. The red dashed lines indicate the FBZ, with the **K** and **K′** valleys at its vertices forming two triangular sub-lattices. (c) Electric field (top) and vector potential (bottom), in atomic units, of a 30 fs long pulse carried at $\lambda_L = 3$ μm and with field strength $F = 0.3$ V/Å. The black dots indicate the peak of the electric field, which coincide with the zero of the vector potential. (d) Electron populations (normalized at each **k**) in the first conduction band of hBN after the pulse in (c).

Fig. 2. (a) Electric field (top) and vector potential (bottom) in a linearly polarized single-cycle pulse, $\lambda = 3$ μm, peak field 1.1 V/Å. The black dots indicate the times when the electric field peaks and electron injection occurs mostly, corresponding to a non-zero vector potential amplitude $A_L^{inj.}$. (b) Conduction band electron populations (normalized at each **k**) after the **ΓK**-polarized pulse in (a). Arrows indicate the streaking, from the minimum band gap crystal momenta $\mathbf{k}_0$ to $\mathbf{k} = \mathbf{k}_0 - A_L^{inj.}$.

[17–19,22]. Recent work has pointed out that the use of single-cycle pulses can lead to asymmetric electron momentum distributions in the neighboring of the **K** and **K′** points of graphene and gapped-graphene systems [24,25]. Here, we demonstrate that intense, few-cycle, linearly polarized pulses can drive the electron population between valleys, inducing a high degree of valley polarization. The mechanism for inducing valley polarization is non-material-specific, independent of the Berry curvature, and can be controlled on a sub-cycle timescale by the CEP of the few-cycle driver. This valley polarization can be read all-optically from the high harmonic spectrum of a probe field, without destroying the valley state.

We first consider hBN described by two bands [16], but the concept and physics are general. At the end, we apply it to MoS_2 described by 22 bands, and in Supplement 1, we consider hBN with eight bands. Our numerical method is described in [9,26]. Briefly, we first obtain the band structure and the transition dipoles from first principles, using density functional theory. For hBN, we use an Heyd–Scuseria–Ernzerhof (HSE06) functional and a 12 × 12 × 4 k-grid, which gives a band gap of 6 eV, which compares well with the experimentally measured value [27]. For MoS_2, we use a Perdew–Burke-Ernzerhof (PBE) functional and an 8 × 8 × 2 k-grid, which gives a minimum band gap of 1.6 eV, in reasonable agreement to that reported [20]. We then transform the Bloch basis into a basis of maximally localized Wannier functions using the Wannier90 code [28], projecting onto the p_z orbitals of boron and nitride for hBN (two bands) and onto the d orbitals of molybdenum and p orbitals of sulfur for MoS_2, including spin (22 bands). The ground state density matrix is constructed as a mixed state with no coherence between the states, where the valence bands are fully occupied. Using the density matrix equations, the initial state is propagated under the influence of the electric field in the length gauge. Our single-active electron approach does not consider exciton formation. Even if excitonic effects are known to be strong in monolayers in the resonant regime, under low-frequency, strong fields, they are expected to be weak, in the same way as in
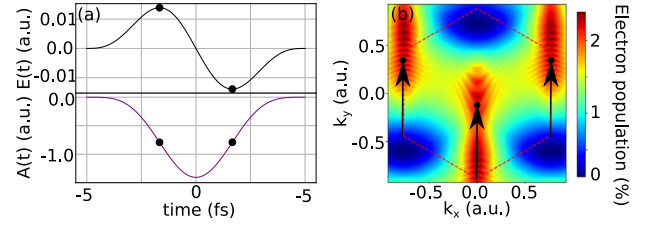
atomic physics the influence of Rydberg states leads to small corrections to the widely used strong-field approximation [29–31]. Many-body effects, as well as macroscopic propagation effects, are included in a phenomenological dephasing time T_2 [32]. Due to the longer timescale, population relaxation during the short pulse is neglected.

Figures 1(a) and 1(b) show the band structure and the Berry curvature of two-band hBN in the first conduction band, illustrating the energy minima and the opposite Berry curvatures at the **K** and **K′** valleys. Consider first the effect of a 30 fs, 3 μm linearly polarized pulse with modest field strength of $F = 0.3$ V/A [Fig. 1(c)]. After the pulse, we extract the **k**-resolved electron populations in the first Brillouin zone (FBZ) of the conduction band, shown in Fig. 1(d). This observable can be extracted with angle-resolved photo-emission spectroscopy (ARPES). As expected, there is no valley polarization: linearly polarized fields, formed by equal superposition of right and left circular drivers, couple equally to both valleys.

Consider now few-cycle pulses, starting with the single-cycle pulse in Fig. 2(a), which allows us to illustrate the relevant physics in the most transparent manner. We shall turn to more realistic pulses in Fig. 3. Figure 2(b) shows results of our simulations for $\lambda = 3$ μm and peak electric field of $E = 1.1$ V/Å, corresponding to a fluence of $F = 0.13$ J/cm^2 for the ~8 fs duration pulse. To our knowledge, there is no experimental study of the damage threshold of monolayer hBN; however, that of graphene was reported to be $F = 0.2$ J/cm^2 [33]. In contrast to the long-pulse regime, Fig. 2(b) shows strong valley polarization.

To understand this result, we note that the carrier frequency of the pulse is well below the bandgap of the material. In this regime, electrons are injected into the conduction band near the instantaneous maxima t_0 of the electric field, marked with black dots in Fig. 2(a). Also, the injection occurs near the minima of the bandgap, hence initiating the population in the **K** and **K′** valleys. There is no preference between the two valleys during the injection. Charge injection is followed by light-driven acceleration of electrons and holes inside the bands. The crystal momentum becomes $\mathbf{k}(t) = \mathbf{k}(t_0) + \mathbf{A}_L(t) - \mathbf{A}_L(t_0)$, where $\mathbf{A}_L(t)$ is the laser vector potential, and the crystal momentum at the moment of injection $\mathbf{k}(t_0)$ is **K** or **K′**. After the end of the pulse $\mathbf{A}_L(t) = 0$, and hence, the populations should be located around $\mathbf{k}_1(t \rightarrow \infty) = \mathbf{K} - \mathbf{A}_L(t_0)$ and $\mathbf{k}_2(t \rightarrow \infty) = \mathbf{K}' - \mathbf{A}_L(t_0)$.

In long pulses, the maxima of the electric field coincide with the zeroes of the vector potential and $\mathbf{A}_L(t_0) = 0$, yielding $\mathbf{k}_1(t \rightarrow \infty) = \mathbf{K}$ and $\mathbf{k}_2(t \rightarrow \infty) = \mathbf{K}'$ with equal population,
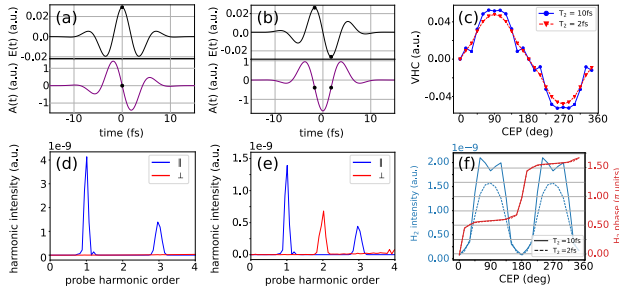
Fig. 3. (a), (b) Electric field (top) and vector potential (bottom) with $\lambda = 3$ μm, peak field 1.5 V/Å, for CEP of (a) 0° and (b) 90°. (c) CEP control of the valley asymmetry defined by Eq. (1) for two dephasing times $T_2 = 10$ fs (blue) and 2 fs (red). (d), (e) HHG spectrum of a probe field that comes after the pulses in (a) and (b), respectively, showing the parallel (blue) and perpendicular (red) components to the probe polarization axis. (f) Intensity (blue) and phase (red) of second harmonic of the probe with respect to the CEP of the few-cycle pulse.

as seen in Fig. 1. In few-cycle pulses, however, the vector potential does not necessarily vanish at the peaks of the electric field. In fact, the two field peaks in Fig. 2(a) correspond to *the same, non-zero, value of the vector potential*. In our simple picture, final electron populations should cluster around $\mathbf{k}_1 = \mathbf{K} - \mathbf{A}_L(t_0)$ and $\mathbf{k}_2 = \mathbf{K}' - \mathbf{A}_L(t_0)$ [black circles in Fig. 2(b)] for the field oriented along $\mathbf{\Gamma K}$. If $\mathbf{A}_L(t_0) = \mathbf{K} - \mathbf{\Gamma}$, then $\mathbf{k}_1 = \mathbf{\Gamma}$ and $\mathbf{k}_2 = \mathbf{K}$, leading to a high degree of valley polarization, as seen in Fig. 2(b). Due to the symmetry of the lattice, the valley polarization will remain zero when the field is polarized along $\mathbf{\Gamma M}$.

Results for more practical few-cycle pulses are shown in Fig. 3. Figs. 3(a) and 3(b) show two pulses for the two different CEP values, CEP = 0° (a) and CEP = 90° (b). The pulses are carried at a central wavelength $\lambda = 3$ μm, with the peak field of $E = 1.5$ V/Å, corresponding to $F = 0.24$ J/cm². Though the chosen fluence is slightly higher than the damage threshold of graphene, we expect hBN, a wide-gap semiconductor, to have a higher threshold. This is supported by the small (8%) electron population excited by the field into the conduction band (Supplement 1). Calculations for weaker field strengths and different pulse envelopes are given in Supplement 1 and do not change the main results. When CEP = 0°, the electric field has a single dominant peak and the vector potential is zero at this peak, which leads to no valley polarization. As the CEP is varied, the value of the vector potential at the field peaks changes, controlling the valley polarization. Figure 3(c) shows CEP control of the valley Hall conductivity (VHC) at the end of the few-cycle pulse $t = t_f$, defined as

$$\sigma_{xy}(t = t_f) = -\frac{e}{\hbar} \sum_n \int_{BZ} \frac{d\mathbf{k}}{(2\pi)^3} f_n(\mathbf{k}, t = t_f) \Omega_n(\mathbf{k}), \quad (1)$$

where $f_n(\mathbf{k}, t)$ and Ω_n are the time-dependent k-resolved population and field-free Berry curvature of band n, respectively. For equal valley population, σ_{xy} is zero since $\Omega_n(\mathbf{k}) = -\Omega_n(-\mathbf{k})$, and grows with increasing valley polarization. For systems with inversion and time-reversal symmetry, where $\Omega(\mathbf{k})$ is zero, σ_{xy} vanishes regardless of the valley polarization. For methods that rely on the optical valley selection rule, a zero Berry curvature automatically implies no valley polarization. This is not the case in our approach. Since the mechanism by which we induce valley polarization does not depend on $\Omega(\mathbf{k})$, it is possible to measure a zero VHC while

having strong valley polarization, e.g., in inversion-symmetric materials.

While the overall dynamics in few-cycle pulses is more complex than in the single-cycle pulse, Fig. 2(a), due to the interference of multiple injection events and multiple Bragg scatterings, substantial VHC can be achieved and controlled by varying the CEP. The blue curve in Fig. 3(c) shows results for a dephasing time of $T_2 = 2$ fs, well below the period of the field, while the orange curve is obtained for $T_2 = 10$ fs, corresponding to the field period. Both situations show clear valley control. For the field parameters chosen, valley polarization maximizes for CEP = 90°, as in Fig. 2, and vanishes for CEP = 0°, when the vector potential at the peak of the field is equal to zero, as expected from the above analysis. The VHC reaches a value of $\sigma_{xy} = 0.052$ a.u., which can be compared to that obtained with a circularly polarized resonant field that excites roughly the same population, which we find to be $\sigma_{xy} = 0.13$ a.u. To maximize the contrast in Fig. 2(c), $\mathbf{A}_L(t_0)$ has to be on the order of the $\mathbf{K} - \mathbf{K}'$ separation.

We now show how the induced valley polarization can be measured all-optically using high harmonic emission. Such emission can be triggered by either the driving few-cycle pulse itself or by a delayed probe pulse. When the dephasing time is shorter than the period of the pulse, the helicity of the harmonics of the driving few-cycle pulse reflects the valley polarization, influenced by the Berry curvature (see Supplement 1). However, this approach is not applicable for dephasing times longer than the field period. Using a delayed probe field strong enough to generate a perpendicular anomalous current offers an alternative solution, mapping the valley polarization onto the helicity of the low-energy harmonics of the field [23]. However, such a strong probe destroys the valley state. Furthermore, both reading mechanisms above require a non-zero Berry curvature, so they are not suited for inversion-symmetric materials.

The valley polarization generated by the strong, few-cycle pulse breaks the symmetry along the $\mathbf{\Gamma K}$ direction. The strength of this symmetry breaking is directly proportional to the valley polarization and can be probed by the even harmonics of a weak probe field [11,34,35], coming after the few-cycle driver. The gapped hexagonal monolayer in its ground state has mirror symmetry along the $\mathbf{\Gamma M}$ direction [Figs. 1(a) and 1(b)]. In the absence of laser-induced symmetry breaking, i.e., valley polarization, a laser polarized along $\mathbf{\Gamma M}$ will not show even harmonics perpendicular to laser polarization [11]. If valley asymmetry is present, even harmonics will show along the perpendicular direction ($\mathbf{\Gamma K}$). To separate the harmonics of the probe from those of the driver, we use a central frequency four times smaller than that of the fundamental.

Figures 3(d) and 3(e) show the four lowest harmonic orders of a weak probe field ($E = 0.1$ V/Å), polarized along $\mathbf{\Gamma M}$, for CEP = 0° (d) and CEP = 90° (e). The former is the case of no valley polarization, and therefore, no even harmonics are present. The latter corresponds to maximum valley polarization, and perpendicularly polarized even harmonics appear. To quantify these results, we compute the strength of the second harmonic as a function of CEP [blue line in (f)]. The oscillation of the even harmonic intensity reproduces remarkably well that of the valley polarization, apart from the sign change. To distinguish between valley polarization at $\mathbf{K}$ and $\mathbf{K}'$, we must access the harmonic phase. The red line in (f) shows the phase of the second harmonic at the central energy, which changes by π between valley polarization at $\mathbf{K}$ (CEP = 90°) and $\mathbf{K}'$ (CEP = 270°).
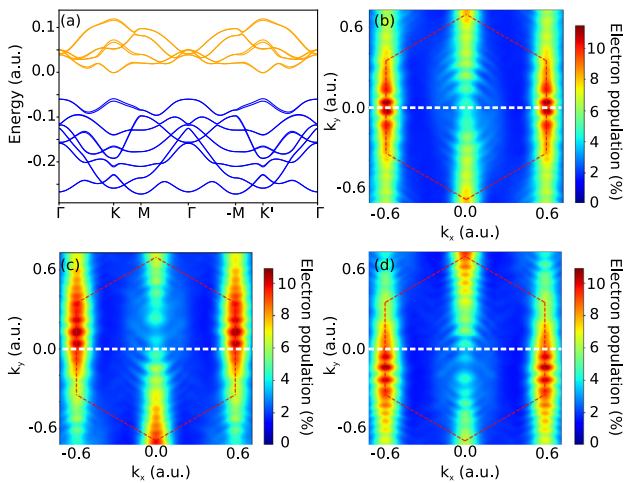
Fig. 4. (a) Band structure of MoS_2, including 14 valence bands (blue) and eight conduction bands (orange). (b)–(d) Sum of electron populations (normalized to each $\mathbf{k}$) in all of the conduction bands after the interaction with a single-cycle pulse with CEP $= 0°$, $90°$, and $270°$, respectively (see text for details). White dashed line at $\mathbf{\Gamma M}$ helps visualize the $\mathbf{K} - \mathbf{K'}$ asymmetry.

Sub-cycle valley selection via single-cycle pulses is expected to work also in TMDs, even if more bands contribute. To test this, we performed simulations in MoS_2, including 22 bands [Fig. 4(a)]. We used a pulse with $E = 0.32$ V/Å and $\lambda = 8$ μm, below the damage threshold [11]. Figures 4(b)–4(d) show the sum of the electron momentum distributions in all of the conduction bands (40% of the excited population resides in the two lowest bands), for CEP $= 0°$, $90°$, and $270°$. Due to the many band crossings, it is hard to accurately compute the VHC. However, it is clear that the $\mathbf{K} - \mathbf{K'}$ asymmetry in the electron momentum distributions can be controlled by the CEP.

In conclusion, we have demonstrated that few-cycle linearly polarized pulses can induce a high degree of valley polarization. The mechanism to induce such polarization does not rely on the optical selection rules, and therefore can be in principle used in inversion symmetric materials, such as TMD bilayers or graphene, opening a new way for implementing ultrafast valleytronic devices. This method should be possible to realize with the existing ultrafast laser technology [1,2,14]. Our approach takes advantage of the sub-cycle control of the electron motion by controlling the oscillations of the electric field under the envelope, and allows for full control of the valley initialization step on a few-femtosecond timescale. The VHC can be measured from the high harmonic emission spectrum.

Disclosures. The authors declare no conflicts of interest.

Supplemental document. See Supplement 1 for supporting content.

REFERENCES

1. A. Baltuška, T. Udem, M. Uiberacker, M. Hentschel, E. Goulielmakis, C. Gohle, R. Holzwarth, V. S. Yakovlev, A. Scrinzi, T. W. Hänsch, and F. Krausz, Nature **421**, 611 (2003).

2. A. Wirth, M. T. Hassan, I. Grguras, J. Gagnon, A. Moulet, T. T. Luu, S. Pabst, R. Santra, Z. A. Alahmed, A. M. Azzeer, V. S. Yakovlev, V. Pervak, F. Krausz, and E. Goulielmakis, Science **334**, 195 (2011).

3. S. Ghimire, A. D. DiChiara, E. Sistrunk, P. Agostini, L. F. DiMauro, and D. A. Reis, Nat. Phys. **7**, 138 (2010).

4. M. Hohenleutner, F. Langer, O. Schubert, M. Knorr, U. Huttner, S. W. Koch, M. Kira, and R. Huber, Nature **523**, 572 (2015).

5. G. Vampa, T. J. Hammond, N. Thiré, B. E. Schmidt, F. Légaré, C. R. McDonald, T. Brabec, D. D. Klug, and P. B. Corkum, Phys. Rev. Lett. **115**, 193603 (2015).

6. O. Schubert, M. Hohenleutner, F. Langer, B. Urbanek, C. Lange, U. Huttner, D. Golde, T. Meier, M. Kira, S. W. Koch, and R. Huber, Nat. Photonics **8**, 119 (2014).

7. F. Langer, M. Hohenleutner, U. Huttner, S. W. Koch, M. Kira, and R. Huber, Nat. Photonics **11**, 227 (2017).

8. R. E. F. Silva, I. V. Blinov, A. N. Rubtsov, O. Smirnova, and M. Ivanov, Nat. Photonics **12**, 266 (2018).

9. R. E. F. Silva, Á. Jiménez-Galán, B. Amorim, O. Smirnova, and M. Ivanov, Nat. Photonics **13**, 849 (2019).

10. N. Yoshikawa, T. Tamaya, and K. Tanaka, Science **356**, 736 (2017).

11. H. Liu, Y. Li, Y. S. You, S. Ghimire, T. F. Heinz, and D. A. Reis, Nat. Phys. **13**, 262 (2017).

12. E. Goulielmakis, V. S. Yakovlev, A. L. Cavalieri, M. Uiberacker, V. Pervak, A. Apolonski, R. Kienberger, U. Kleineberg, and F. Krausz, Science **317**, 769 (2007).

13. F. Krausz and M. Ivanov, Rev. Mod. Phys. **81**, 163 (2009).

14. T. Higuchi, C. Heide, K. Ullmann, H. B. Weber, and P. Hommelhoff, Nature **550**, 224 (2017).

15. K. S. Novoselov, A. K. Geim, S. V. Morozov, D. Jiang, Y. Zhang, S. V. Dubonos, I. V. Grigorieva, and A. A. Firsov, Science **306**, 666 (2004).

16. A. H. Castro Neto, F. Guinea, N. M. R. Peres, K. S. Novoselov, and A. K. Geim, Rev. Mod. Phys. **81**, 109 (2009).

17. D. Xiao, W. Yao, and Q. Niu, Phys. Rev. Lett. **99**, 236809 (2007).

18. J. R. Schaibley, H. Yu, G. Clark, P. Rivera, J. S. Ross, K. L. Seyler, W. Yao, and X. Xu, Nat. Rev. Mater. **1**, 16055 (2016).

19. S. A. Vitale, D. Nezich, J. O. Varghese, P. Kim, N. Gedik, P. Jarillo-Herrero, D. Xiao, and M. Rothschild, Small **14**, 1801483 (2018).

20. K. F. Mak, K. L. McGill, J. Park, and P. L. McEuen, Science **344**, 1489 (2014).

21. S. A. Oliaei Motlagh, J.-S. Wu, V. Apalkov, and M. I. Stockman, Phys. Rev. B **98**, 081406 (2018).

22. F. Langer, C. P. Schmid, S. Schlauderer, M. Gmitra, J. Fabian, P. Nagler, C. Schüller, T. Korn, P. G. Hawkins, J. T. Steiner, U. Huttner, S. W. Koch, M. Kira, and R. Huber, Nature **557**, 76 (2018).

23. Á. Jiménez-Galán, R. E. F. Silva, O. Smirnova, and M. Ivanov, Nat. Photonics **14**, 728 (2020).

24. C. Lefebvre, D. Gagnon, F. Fillion-Gourdeau, and S. MacLean, J. Opt. Soc. Am. B **35**, 958 (2018).

25. S. A. O. Motlagh, F. Nematollahi, A. Mitra, A. J. Zafar, V. Apalkov, and M. I. Stockman, J. Phys. Condens. Matter **32**, 65305 (2019).

26. R. E. F. Silva, F. Martín, and M. Ivanov, Phys. Rev. B **100**, 195201 (2019).

27. K. Watanabe, T. Taniguchi, and H. Kanda, Nat. Mater. **3**, 404 (2004).

28. A. A. Mostofi, J. R. Yates, Y.-S. Lee, I. Souza, D. Vanderbilt, and N. Marzari, Comput. Phys. Commun. **178**, 685 (2008).

29. M. Lewenstein, P. Balcou, M. Y. Ivanov, A. L'Huillier, and P. B. Corkum, Phys. Rev. A **49**, 2117 (1994).

30. E. Pisanty and Á. Jiménez-Galán, Phys. Rev. A **96**, 063401 (2017).

31. J. A. Pérez-Hernández, L. Roso, and L. Plaja, Opt. Express **17**, 9891 (2009).

32. I. Floss, C. Lemell, G. Wachter, V. Smejkal, S. A. Sato, X.-M. Tong, K. Yabana, and J. Burgdörfer, Phys. Rev. A **97**, 11401 (2018).

33. A. Roberts, D. Cormode, C. Reynolds, T. Newhouse-Illige, B. J. LeRoy, and A. S. Sandhu, Appl. Phys. Lett. **99**, 051912 (2011).

34. Á. Jiménez-Galán, N. Zhavoronkov, M. Schloz, F. Morales, and M. Ivanov, Opt. Express **25**, 22880 (2017).

35. T. T. Luu and H. J. Wörner, Nat. Commun. **9**, 916 (2018).